Original Article

DOI: 10.5582/ddt.2025.01102

Zhimu-Huangbo ameliorates AQP4 depolarization in diabetic cognitive impairment rats by targeting the serum-derived exosomal TIMP3-mediated MMP9/β-DG pathway

Ying Li[1,2,§], Xueling Lin[1,2,§], Jie Bu[1,2], Genhui Yang[1,2], Lin Niu[1,2], Lin Zhang[1], Dingbin Liu[5], Yanjun Zhang[1,2,3,4,*], Qingsheng Yin[1,2,*], Pengwei Zhuang[1,2,3,4,*]

[1] State Key Laboratory of Chinese Medicine Modernization, Tianjin University of Traditional Chinese Medicine, Tianjin, China;
[2] Haihe Laboratory of Modern Chinese Medicine, Tianjin University of Traditional Chinese Medicine, Tianjin, China;
[3] First Teaching Hospital of Tianjin University of Traditional Chinese Medicine, Tianjin, China;
[4] National Clinical Research Center for Chinese Medicine Acupuncture and Moxibustion, Tianjin, China;
[5] Nankai University, Tianjin, China.

SUMMARY: Aquaporin-4 (AQP4) depolarization-mediated glymphatic system (GS) dysfunction is a critical pathological mechanism in diabetic cognitive impairment (DCI). However, its underlying mechanism has not been clarified. The Zhimu-Huangbo (ZMHB) herb pair, a classic formulation historically employed in traditional Chinese medicine, demonstrates neuroprotective effects, including the amelioration of cognitive dysfunction. Emerging evidence suggests that the exosomal pathway may regulate abnormalities in diabetes-induced AQP4 polarization. Nevertheless, whether the neuroprotective effects of ZMHB mediate the restoration of AQP4 polarity through the exosomal pathway remains to be elucidated. This study takes the exosomal pathway as the entry point to elucidate the mechanism of AQP4 depolarization in DCI and determine how ZMHB restores AQP4 polarization and improves cognitive function. ZMHB significantly improved cognitive function, effectively restored GS function and maintained AQP4 polarization. Pharmacological blockade of exosomal pathways partially reduced the therapeutic effects of ZMHB, demonstrating that its efficacy depends on exosome-mediated signaling; proteomics combined with western blotting validation revealed tissue inhibitor of metalloproteinase 3 (TIMP3) as a pivotal protein modulated by ZMHB, which restored AQP4 polarization by inhibiting matrix metalloproteinase-9 (MMP9) activity and blocking β-dystroglycan (β-DG) cleavage in astrocytes. *In vitro* studies further demonstrated that both ZMHB-treated serum exosomes (ZMHB-sExos) and the TIMP3 agonist MPT0B390 restored astrocytic AQP4 polarization by modulating the MMP9/β-DG pathway. We demonstrated that ZMHB restored AQP4 depolarization in DCI rats by modulating the exosomal TIMP3-MMP9/β-DG pathway.

Keywords: Zhimu-Huangbo, diabetic cognitive impairment, glymphatic system, exosomes, AQP4, TIMP3

1. Introduction

Diabetes is a chronic metabolic disease that is characterized by persistent hyperglycemia and insulin resistance. Cognitive impairment is a common complication of diabetes (*1-3*), affecting 25–35% of diabetic patients and increasing their risk of cognitive decline by 1.5–2.5 times compared with nondiabetic individuals (*4,5*). Unfortunately, the incomplete understanding of diabetic cognitive impairment (DCI) pathogenesis has resulted in the absence of U.S. Food and Drug Administration (FDA)-approved drugs to clinically treat this condition.

Impaired glymphatic system (GS) function, characterized by diminished clearance of neurotoxic metabolites, underlies the pathogenesis of DCI (*6-8*). The clearance capacity of the GS critically depends on the polarized distribution of aquaporin-4 (AQP4) at perivascular astrocytic endfeet (*9,10*), and AQP4 depolarization may represent a pivotal factor in DCI pathogenesis. Previous studies have indicated that exosomes restore GS function by modulating AQP4 polarization, but the detailed mechanism remains unknown. Under pathological diabetic conditions, aberrant protein expressions in exosomes may exacerbate cognitive deficits (*11*). Notably, whether circulating serum-derived exosomes, as essential protein-delivery vehicles (*12*), mediate DCI progression by regulating

cerebral AQP4 polarization and GS functional integrity has not been fully investigated.

The distribution of AQP4 polarization is partially dependent on β-dystroglycan (β-DG), while matrix metalloproteinase-9 (MMP9) acts on specific polysaccharide structures within β-DG through its active enzymatic sites, leading to β-DG cleavage or defects and affecting the localization and function of AQP4 (*13*). Importantly, the tissue inhibitor of metalloproteinase 3 (TIMP3) is a natural inhibitor of MMP9 that inhibits the activity of MMP9 and protects β-DG from degradation, thus supporting the polarization and function of AQP4 (*14,15*). Research has shown that the absence of β-DG after DCI leads to the loss of AQP4 polarization, thereby exacerbating cognitive impairment (*16*). Therefore, investigating whether TIMP3 improves cognitive function by regulating the MMP9/β-DG pathway and affecting AQP4 polarization in DCI models is necessary.

According to traditional Chinese medicine (TCM), DCI is recognized as a chronic disorder that is primarily attributed to the pathogenic mechanism of "toxin damaging brain collaterals", with "heat clearing and detoxification" serving as its fundamental therapeutic strategy. Leveraging the unique advantages of TCM in the multipathway and multitarget regulation of complex diseases, Tong Guan Wan, a classic formula composed of Anemarrhenae Rhizoma (Zhimu, dried rhizome of *Anemarrhena asphodeloides* Bunge) and Phellodendri Chinensis Cortex (Huangbo, dried bark of *Phellodendron chinense* C.K.Schneid.); this formula is described in the Yuan Dynasty text Secret Record of the Chamber of Orchids (*17,18*). Zhimu, characterized by its cold nature and moistening properties, excels in nourishing Yin, moistening dryness, clearing heat, and purging fire. Huangbo is bitter and cold in nature, excelling at purging fire and detoxifying. Both herbs act on the kidney meridian, exhibiting synergistic interactions: they mutually increase heat-clearing and fire-purging effects while maintaining a dynamic equilibrium between Yin-nourishing and damp-drying, thereby preventing Yin impairment caused by bitter-cold properties. This collaboration achieves Yin-nourishing, heat-clearing, and detoxification effects. Recent studies have shown that "bitter-cold" herbs exhibit heat-clearing and detoxification functions that significantly enhance neural protection by increasing neuronal vitality and promoting neural repair (*19*). Importantly, previous research has shown that the herb pair ZMHB, a commonly used heat-clearing and detoxifying formulation, can significantly increase the learning and memory abilities of DCI mice (*20,21*). However, whether ZMHB improves cognitive function by regulating AQP4 polarization remains unclear.

Therefore, in this study, the exosome release inhibitor GW4869 was used to confirm the essential role of the exosomal pathway in the ZMHB-mediated improvement in AQP4 polarization. Serum exosomal proteomics was performed to identify differentially expressed proteins and pinpoint key regulatory proteins, and western blotting and immunofluorescence staining were used to evaluate the effects of ZMHB on the TIMP3-MMP9/β-DG pathway. Furthermore, ZMHB-treated serum exosomes (ZMHB-sExos) and the TIMP3-specific agonist MPT0B390 were applied to astrocytes, revealing the targeted regulatory role of the TIMP3-MMP9/β-DG pathway in the distribution of polarized AQP4 at the molecular mechanism level. Overall, these studies revealed the underlying mechanism by which ZMHB restores AQP4 polarization in DCI rats through modulating the exosomal TIMP3-mediated MMP9/β-DG pathway, thereby providing a novel therapeutic strategy for clinical intervention in DCI. The graphical abstract below visually illustrates the overall framework of the DCI pathological mechanisms and the protective effects of ZMHB (Figure S1).

2. Materials and Methods

2.1. Preparation of ZMHB

Zhimu (dried rhizome of *Anemarrhena asphodeloides* Bunge) was purchased from Beijing Bencao Fangyuan Pharmaceutical Group Co., Ltd. (origin Hebei Province, China, Batch No.20150136). Huangbo (dried bark of *Phellodendron Chinense* C.K.Schneid.) was purchased from Beijing Bencao Fangyuan (BoZhou) Pharmaceutical Technology Co., Ltd. (origin Sichuan Province, China; batch no. 20160125). Herbs were extracted 3 times by reflux with 8× 80% ethanol at a ratio of 1:1, each time for 2 h, filtered, and the filtrate was removed. The drug extract was concentrated to 0.36 g/mL with a rotary evaporator and stored in a refrigerator at -20°C.

2.2. Chemical component analysis of ZMHB

For quality assurance, ultra-high performance liquid chromatography quadrupole-time-of-flight mass spectrometry (UPLC–Q–TOF–MS) was used to analyze the chemical profile of ZMHB. The ZMHB extract was diluted to 0.1 g/mL. A Waters ACQUITY UPLC BEH C18 (2.1 mm × 50 mm, 1.7 μm) was used for separation. The mobile phase consisted of water (A) and acetonitrile (B), with a column temperature of 45°C and an injection volume of 5 μL; the flow rate was set at 0.3 mL/min. The gradient profile was:0–0.5 min (A:95%; B:5%), 0.5–6 min (A:80%; B:20%), 6–8 min (A:78%; B:22%), 8–13 min (A:62%; B:38%), 13–18 min (A:50%; B:50%), 18–26 min (A:0%; B:100%), and 26–30 min (A:98%; B:2%). Positive ion and negative ion modes were used for data collection. The positive ion mode was as follows: source temperature (120°C), desolvation temperature (450°C), capillary voltage (3 kV), collision energy (30–50 V), desolvation (800 L/h), cone gas (50 L/h), and scan range

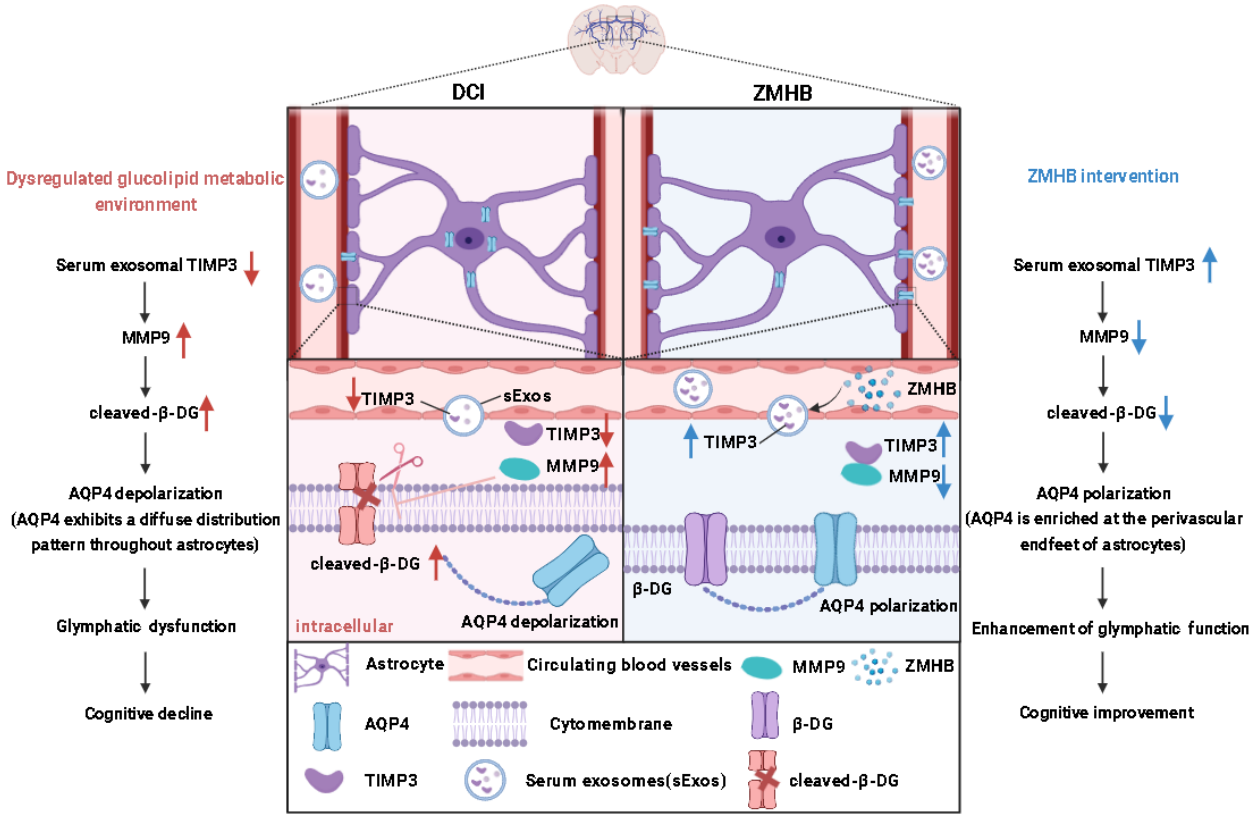

Figure S1. Schematic representation of DCI pathogenesis and the protective actions of ZMHB.

(50–1,200 m/z). The negative ion mode was as follows: source temperature (120°C), desolvation temperature (400°C), capillary voltage (2 kV), collision energy (30–50 V), desolvation (800 L/h), cone gas (50 L/h), and scan range (50–1,200 m/z). The data were processed using MassLynx™4.1 software.

2.3. Experimental animals

Wistar rats (n = 120, male, 4 weeks old) were purchased from Beijing Vital River Laboratory Animal Technology Co., Ltd. (SCXK (Jing) 2018-0006) and raised in the SPF-level barrier laboratory of the Animal Center of Tianjin University of Traditional Chinese Medicine. The temperature of the feeding room was 21 ± 2°C, the air pressure was constant, the animals were subjected to alternating day and night conditions of 12 h each, and food and water were freely available. This study passed the ethical review for animal experiments at Tianjin University of Traditional Chinese Medicine (TCM-LAEC2021152). The welfare of the laboratory animals was ensured by following the Laboratory Animal Guidelines for Ethical Review of Animal Welfare (GB/T 35892-2018).

2.4. Induction of the diabetic model and therapeutic intervention

The rats (n = 60) were acclimatized to laboratory conditions for one week prior to experimentation. Cognitive performance was evaluated using a Morris water maze (MWM; Anhui Zhenghua Biotechnology, Anhui, China), with 3 rats excluded because they demonstrated congenital frailty, locomotor impairments, or nonnavigational swimming patterns. The remaining experimental rats were randomly divided into a Control (Con) group (n = 12) and a model group (n = 45). The Con group was fed a normal diet, and the model group was fed a high-fat diet (HFD; Beijing Xiaoshu Youtai Biotechnology Co., Ltd., Beijing, China, D12492) for three weeks. After fasting for 12 h, the model group received 35 mg/kg intraperitoneal injections of streptozotocin (STZ, Sigma-Aldrich, St. Louis, MO, USA, S0130) three times, with an interval of 2 days between each injection. The Con group was injected with only an equal amount of citric acid sodium citrate buffer (pH 4.5, 0.1 mol/L, Solarbio, Beijing, China, C1013) under the same conditions. One week later, rats whose fasting blood glucose (FBG) concentrations exceeded 16.7 mmol/L, taken from their tail veins, were selected as diabetes model rats for subsequent experiments. The abovementioned screened rats (n = 36) were randomly divided into three groups: the DCI group, the ZMHB low-dose (ZMHB-L) group (2.16 g/kg, ig), and the ZMHB high-dose (ZMHB-H) group (4.32 g/kg, ig), with 12 rats in each group.

To determine whether ZMHB could prevent and treat cognitive impairment by regulating the exosomes,

an additional ZMHB + exosome release inhibitor GW4869 (MedChemExpress, NJ, USA, HY-19363) group (4.32 g/kg, ig + 1 mg/kg, ip) was added. The cognitive performance of the rats (n = 60) was initially assessed using the MWM test, and 2 rats were excluded because of congenital weakness, motor dysfunction, or nonnavigational swimming patterns. The remaining rats were randomly divided into a Con group (n = 12) and a model group (n = 46). A diabetic model was induced using STZ combined with a HFD, and 10 rats with FBG concentrations less than 16.7 mmol/L were excluded. The final selected rats (n = 36) were randomly divided into three groups: the DCI group, the ZMHB group (4.32 g/kg, ig), and the ZMHB + exosome release inhibitor GW4869 group (4.32 g/kg, ig + 1 mg/kg, ip), with 12 rats in each group. ZMHB was administered continuously for 8 weeks; the Con and DCI groups were given equal amounts of physiological saline orally once a day for a total of 8 weeks; in the combination group, GW4869 was injected intraperitoneally every other day. It has been reported in the literature that diabetic rats exhibit obvious symptoms of cognitive impairment symptoms after 8 weeks of modeling. Therefore, this experiment was conducted 8 weeks in advance before DCI was established (*22,23*).

The basis for calculating the 2-fold clinically equivalent dose of ZMHB (4.32 g/kg) was as follows: Based on the recommended human dosages of Zhimu and Huangbo that were provided in the Pharmacopoeia of the People's Republic of China (2020 edition) (total crude drug: 24 g; ratio: Zhimu 12 g; Huangbo 12 g), the clinically equivalent dose for rats was derived using the following human-to-rat dose conversion formula: Rat dose (g/kg) = Human dose (g)/70 kg (standard human body weight) × 6.3 (conversion factor). This yielded a rat-equivalent dose of 2.16 g/kg, and the 2-fold clinically equivalent dose was accordingly 4.32 g/kg.

2.5. Weight and fasting blood glucose

During the administration period, the body weights and FBG levels (after a fasting period from 8:00 PM on the previous day to 8:00 AM the next day) of the rats in each group were measured at four-week intervals, and the dynamic changes in their body weights and FBG levels were observed.

2.6. Morris water maze

The MWM test was used to evaluate the learning and memory abilities of the experimental animals. Within the time range of the learning and memory test on Days 1–5, the rats were allowed to swim in a dark pool, which was 150 cm in diameter and 50 cm in height, for 60 s to find the target platform (10 cm diameter) located in the center of one quadrant. If the platform was not found after 60 s of swimming, the rats were gently guided to the platform and allowed to redirect to the remote visual prompt for 20 s before being removed from the swimming pool. On the 6th day, the target platform was removed, and the rats were allowed to swim freely for 60 s while the time to reach the platform, frequency of crossing the platform, and duration in the zone were recorded.

2.7. Cresol violet staining

Brain tissue samples were fixed, embedded, and sectioned, and changes in the number of hippocampal neurons in each group were observed by cresyl violet staining. The details are as follows: the paraffin sections were dewaxed and dehydrated with xylene and gradient ethanol, rinsed with distilled water, stained with cresyl violet at 60℃ for 30 min, rinsed with running water for 30 s, differentiated with Nissl differentiation solution for 1 min, dehydrated with gradient ethanol and xylene, mounted with neutral resin, and finally observed under a digital slide scanner (3DHISTECH, Budapest, Hungary, Pannoramic MIDI).

2.8. Magnetic resonance imaging

Nest, 10 μL of gadolinium-diethylenetriaminepentaacetic acid (Gd-DTPA) at a concentration of 21 mmol/L was injected into the cerebellomedullary cistern of each experimental animal at a speed of 1.6 μL/min. After the Gd-DTPA injections were complete, the experimental animals were immediately fixed in a small animal magnetic resonance imaging (MRI) fixed slot with set parameters. Continuous scans were performed at 10 min, 20 min, 30 min, 40 min, and 50 min after injection, and the images were saved after scanning (Bruker Biospin, Ettlingen, Germany, Bruker Biospec 70/20 USR, Paravision 6.0). The dynamic exchange of cerebrospinal fluid and interstitial fluid was detected using three-dimensional T1-weighted images (3D T1WIs). 3D T1WIs were obtained with the following parameters: echo time of 2.4 ms, repetition time of 16.63 ms, field-of-view of 2.0 × 2.0 × 1.0 cm, flip angle of 20°, and scanning time of 8 min and 4 s, resulting in a 0.14 × 0.14 × 0.14 mm image. Finally, the MRI data were processed, including the extraction and calibration of the head signal, as well as the percentage of stereo pixels converted into baseline signals using SPM8 software.

2.9. Western blotting

RadioImmunoPrecipitation Assay (RIPA) protein lysis buffer and phenylmethylsulfonyl fluoride (PMSF) were used to extract total protein from the brain at a ratio of 100:1. A Bicinchoninic Acid Assay (BCA) protein concentration assay kit was used for protein quantification. Forty micrograms of protein was electrophoresed *via* 4-12% sodium dodecyl sulfate-polyacrylamide gel electrophoresis (SDS-PAGE),

transferred to a polyvinylidene difluoride (PVDF) membrane and blocked with blocking buffer at room temperature for 20 min. Subsequently, primary antibodies were added and incubated at 4℃ for 12 h. The primary antibodies used in the experiments included rabbit anti-CD81 (Abcam, Cambridge, UK, ab109201, 1:1,000); rabbit anti-TSG101 (CST, Boston, MA, USA, 72312S, 1:1,000); rabbit anti-AQP4 (Santa Cruz Biotechnology, Dallas, TX, USA, sc-390488, 1:1,000); rabbit anti-TIMP3 (Proteintech, Wuhan, Hubei, China, 10858-1-AP, 1:1,000); MS anti-β-DG (Santa Cruz Biotechnology, sc165998, 1:100); rabbit anti-MMP9 (Proteintech, 10375-2-AP, 1:500); MS anti-β-actin (Abcam, ab8226, 1:1,000); and rabbit anti-β-tubulin (Abcam, ab108342, 1:1,000). HRP-labeled secondary antibodies (goat-anti-rabbit IgG; CST, Cat#7074, 1:3,000, and goat anti-MS IgG; Abcam, ab6789, 1:1,000) were added and incubated for 2 h at room temperature, after which the blots were developed using a highly sensitive ECL kit. Image-Pro Plus 6.0 optical density analysis software was used to determine the gray values of the protein bands. β-actin or β-tubulin was used as a loading control. The relative expression level is the ratio of the gray value of the target protein and reference protein.

2.10. Immunofluorescence staining

After dehydration, dewaxing, and antigen repair, the brain tissue sections were incubated with primary antibodies (MS anti-AQP4: Servicebio, Wuhan, Hubei, China, GB12529, 1:500; rabbit anti-GFAP Servicebio, GB11096, 1:500; rabbit anti-CD31: Servicebio, GB113151, 1:200; rabbit anti-TIMP3: Thermo Fisher Scientific, Waltham, MA, USA, PA5-116049, 1:200; MS anti-GFAP: CST, 3970S, 1:400; MS anti-β-DG: Santa Cruz Biotechnology, sc-33702, 1:50; and rabbit anti-AQP4, CST, D1F8E, 1:50) at 4℃ overnight. On the next day, the slices were washed 3 times with PBS and incubated with secondary antibodies (goat-anti-MS IgG: Servicebio, GB21301, 1:300; goat-anti-rabbit IgG: Servicebio, GB25303, 1:400; goat-anti-rabbit IgG: Abcam, ab150077, 1:500; and goat-anti-MS IgG: Abcam, ab150113, 1:500) at room temperature for 2 h. Finally, the slices were washed 3 times with PBS and sealed with an anti-fluorescence quenching agent. Finally, ImageJ software was used to analyze the areas of protein-positive regions.

2.11. Exosome isolation and identification

First, blood was taken from the abdominal aorta of each rat, and the supernatant was collected by centrifugation. The supernatant was subsequently centrifuged at 2,000 × g for 30 min at 4℃. Afterward, the supernatant was transferred to a new centrifuge tube and centrifuged at 12,000 × g for 45 min at 4℃ to remove the largest vesicle, after which the supernatant was filtered through a 0.45 μm filter. The filtrate was subsequently subjected to ultracentrifugation (Beckman Coulter, Brea, CA, USA, Optima XP-CTZ19D16) at 110,000 × g for 2 h at 4℃, followed by resuspension in PBS. The exosomes that were obtained through ultracentrifugation were diluted at a 1:2 ratio and 10 μL of sample and 10 μL of phosphotungstic acid were dropped onto a copper mesh, precipitated for 1 min and dried. The imaging results were obtained through transmission electron microscopy (TEM) under 580 kV conditions. The samples were subsequently subjected to nanoparticle tracking analysis (NTA) and western blotting.

2.12. 4D-Label-free Proteomics

To explore the potential mechanism through which circulating serum exosomes (sExos) from the ZMHB group affect the repair of cognitive damage, 4D label-free quantitative proteomics technology were used to detect macroscopic changes in the expressions of circulating serum proteins in each group. The SDT lysate was added to the processed sExos from each group for protein extraction, and the BCA method was used for protein quantification. Twenty micrograms of protein from each sample were added to an appropriate amount of 5× loading buffer. After 5 min in a water bath, electrophoresis (180 V, 45 min) was performed. Coomassie blue R-250 staining was performed, followed by tryptic digestion using the filter aided sample preparation (FASP) method. The peptide segments were desalinated using a C18 cartridge. After freeze-drying, 40 μL of 0.1% formic acid solution was added for redissolution, and the peptide segments were quantified (OD280). Each group of samples was separated using a nanoElute HPLC system with a nanoliter flow rate. Buffer solution A was a 0.1% formic acid aqueous solution, and solution B was a 0.1% formic acid acetonitrile aqueous solution. The chromatographic column was equilibrated with 95% liquid A, and the samples were separated by C18 reversed-phase analysis at a flow rate of 300 nL/min. After chromatographic separation, a TOF Pro mass spectrometer was used for mass spectrometry analysis, with a positive ion detection method and a scanning range of 100–1,700 m/z. Data were collected in parallel accumulation serial fragmentation (PASEF) mode. Finally, in this study, the label-free algorithm in MaxQuant software (version 1.6.14) was used for nonlabel quantitative analysis of the proteomic data. This experiment was completed by APPLIED Protein Technology.

2.13. Cell line and cell culture

Mouse astrocytes were purchased from Pricella (C8-D1A; Wuhan, Hubei, China) and cultured in low-sugar Dulbecco's Modified Eagle's Medium (DMEM; Gibco,

New York, NY, USA, 11885084) supplemented with 10% fetal bovine serum at 37°C and 5% CO_2.

2.14. Induction of high-glucose-induced cellular injury model

After they reached 80%-90% confluence, 100 μL (5×10^5 cells) of astrocytes were cultured in 96-well plates for 24 h. Subsequently, the cells were cultured in basic medium for 24 h to maintain the same logarithmic growth period. The cultures were subsequently treated with different concentrations of glucose (5, 15, 25, 35, 45, and 55 mM) for 24 h to induce high-sugar damage. After treatment, 10 μL of Cell Counting Kit-8 (CCK-8; Beyotime, Shanghai, China, C0039) was added to each well and incubated at 37°C for 30 min, after which the absorbances were measured at 450 nm using a microplate reader (TECAN, Männedorf, Switzerland).

2.15. MPT0B390 administration concentration screening

To determine the optimal concentration of MPT0B390 (MedChemExpress, HY-145426) for C8-D1A cells, C8-D1A cells were pretreated with serum-free medium for 24 h to achieve cell cycle synchronization. The cells were then exposed to gradient concentrations of MPT0B390 (*e.g.*, 0.01, 0.1, 1, and 2 μM) or the solvent control (0.1% DMSO) for 24 h. Cell viability was subsequently assessed using the CCK-8 assay.

2.16. Exosome labeling and uptake

In accordance with the manufacturer's instructions, PKH26 Fluorescent Cell Linker Kits (Umibio, Shanghai, China, UR52302) were used to label the exosomes. Next, the exosomes (200 μg/mL) were incubated with 5×10^5 astrocytes for 24 h, fixed with 4% formaldehyde for 30 min, stained with DAPI for 15 min, and observed under a fluorescence microscope (KEYENCE, Osaka, Japan).

2.17. Cellular immunofluorescence staining

After cell fixation and goat serum blocking, the cells were incubated with primary antibodies (MS anti-AQP4: Bioss antibodies, Beijing, China, bsm-33068M, 1:100; rabbit anti-TIMP3: Thermo Fisher Scientific, PA5-116049, 1:100; MS anti-β-DG: Santa Cruz Biotechnology, sc-33702, 1:50) at 4°C overnight. On the next day, the 96-well plates were washed 3 times with PBS and incubated with secondary antibodies (goat-anti-rabbit IgG: Abcam, ab150077, 1:500 and goat-anti-MS IgG: Abcam, ab150113, 1:500) at room temperature for 2 h. Finally, the cells were washed 3 times with PBS and sealed with an anti-fluorescence quenching agent. Finally, ImageJ software was used to analyze the areas of TIMP3, AQP4 and β-DG expressions.

2.18. Statistical analysis

The experimental data are presented as the means ± SDs and were analyzed using SPSS 29.0 statistical software. Escape latency data were analyzed by repeated-measures analysis of variance. One-way ANOVA was used for normally distributed data, whereas the Kruskal-Wallis test was used for abnormally distributed data. A *P* value less than 0.05 was used to indicate statistical significance. All the data were plotted using GraphPad Prism 8 software and assembled using Adobe Photoshop CS6 software.

3. Results

3.1. Identification of chemical constituents in ZMHB extracts

For quality assurance, we used UPLC–Q–TOF–MS to analyze the chemical profile of ZMHB. The ion chromatograms and detailed information of the ZMHB component analysis are shown in Figure 1 and Table 1. By searching the literature, Traditional Chinese Medicine Database (TCMD) and Traditional Chinese Medicine Systems Pharmacology Database and Analysis Platform (TCMSP), the chemical constituents of ZMHB were summarized. The main components are as follows: mangiferin from Anemarrhenae Rhizoma, and berberine and phellodendrine from Phellodendri Chinensis Cortex.

3.2. ZMHB improved the cognitive function of DCI rats

The procedures for model induction and drug treatment are shown in Figure 2A. We first investigated the effects of ZMHB on body weight and FBG levels in DCI rats. At the endpoint of treatment, our results demonstrated that DCI rats exhibited significantly reduced body weights (Figure 2B) and markedly elevated FBG levels (Figure 2C), which are consistent with the clinical manifestations of patients with type 2 diabetes. Postintervention, the body weights of both ZMHB-L and ZMHB-H tended to increase in DCI rats (Figure 2B). However, neither ZMHB-L nor ZMHB-H reduced the elevated FBG levels in DCI rats (Figure 2C). To investigate the impact of ZMHB on cognitive function in DCI rats, we evaluated spatial learning and memory abilities using the MWM test. Compared with the Con group, the DCI group exhibited longer escape latencies, indicating impaired learning ability (Figure 2D). Notably, the ZMHB-L and ZMHB-H treatments significantly shortened the escape latencies (Figure 2D), suggesting that ZMHB ameliorates DCI-induced learning deficits. In the spatial probe trial (platform removed), DCI rats exhibited prolonged times to first reach the original platform location, whereas ZMHB-treated animals exhibited significantly shorter times

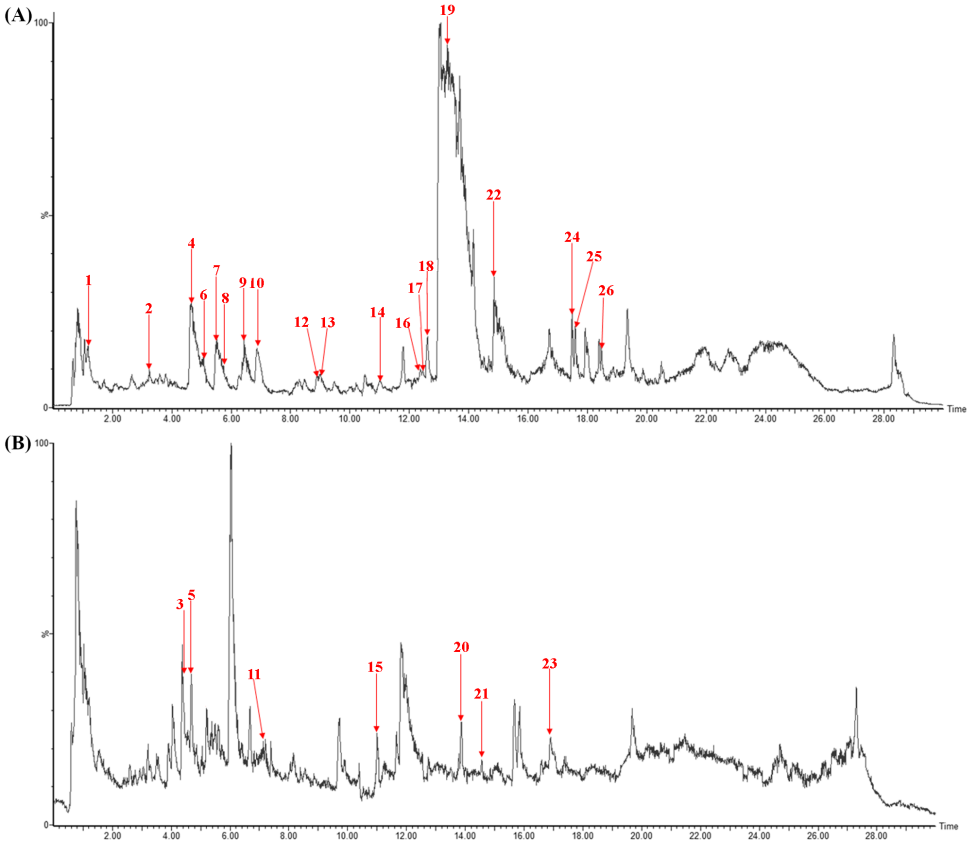

Figure 1. Identification of chemical constituents in ZMHB extracts. (**A**) shows the positive acquisition mode. (**B**) shows the negative acquisition mode.

Table 1. Identification of chemical constituents in ZMHB extracts

No	t/min	Mz	Exact mass	Error	Formula	Name	Plant material
1	1.17	180.1391	181.278	1.14	$C_{11}H_{18}NO$	N-Candicine	Huangbo
2	3.24	585.1458	585.4957	0.35	$C_{25}H_{28}O_{16}$	Neomangiferin	Zhimu
3	4.43	353.0870	353.3056	0.22	$C_{16}H_{18}O_9$	Chlorogenic acid	Huangbo
4	4.65	342.1711	343.4228	1.25	$C_{20}H_{24}NO_4$	Phellodendrine	Huangbo
5	4.69	367.1025	366.3245	-0.80	$C_{17}H_{19}O_9$	Amurenlactone A/B	Huangbo
6	5.07	448.1981	449.5011	1.30	$C_{23}H_{30}NO_8$	7-O_x005f_x005f_x005fglucopyranoside of 1-(p_x0002_hydroxybenzyl)- 6,7-dihydroxy-Nmethylisoquinoline	Huangbo
7	5.41	423.0928	423.3533	0.26	$C_{19}H_{18}O_{11}$	Mangiferin	Zhimu
8	5.63	342.1703	343.4228	1.25	$C_{20}H_{24}NO_4$+	Magnoflorine	Huangbo
9	6.43	369.1196	369.3483	0.23	$C_{17}H_{20}O_9$	3-Feruloylquinic acid	Huangbo
10	6.93	314.1752	314.4045	0.23	$C_{19}H_{23}NO_3$	Lotusine	Huangbo
11	7.21	567.2085	567.5671	0.36	$C_{27}H_{36}O_{13}$	(+/-) 8- (4-Hydroxy_x005f3-methoxyphenyl)- 6,7-bis(hydroxymethyl) -3-methoxy_x0002_5,6,7,8-tetrahydro_x0002_2-naphthalenyl-β-D-glucopyranoside	Huangbo
12	8.90	344.1854	345.4387	1.25	$C_{20}H_{26}NO_4$	Tembetarine	Huangbo
13	9.00	356.1856	356.4418	0.26	$C_{21}H_{25}NO_4$	Menisperine	Huangbo
14	10.99	356.1855	356.4418	0.26	$C_{21}H_{25}NO_4$	Tetrahydropalmati	Huangbo
15	11.03	259.0604	259.2383	0.18	$C_{14}H_{12}O_5$	2,6,4'-trihydroxy-4- methoxybenzophenoe	Zhimu
16	12.39	322.1076	323.3483	1.24	$C_{19}H_{16}NO_4$	Berberrubine	Huangbo
17	12.44	338.1392	339.3911	1.25	$C_{20}H_{20}NO_4$	Columbamine	Huangbo
18	12.61	338.1391	339.3911	1.25	$C_{20}H_{20}NO_4$+	Jatrorrhizine	Huangbo
19	13.27	336.1237	337.3752	1.25	$C_{20}H_{18}NO_4$	Berberine	Huangbo
20	13.86	947.4879	947.0816	-0.40	$C_{46}H_{75}O_{20}$	Timosaponin C	Zhimu
21	14.56	329.2313	329.4570	0.23	$C_{18}H_{34}O_5$	Sanleng acid	Huangbo
22	14.86	903.4950	904.0797	0.58	$C_{45}H_{74}O_{18}$	Timosaponin B	Zhimu
23	16.91	251.1075	251.3049	0.20	$C_{17}H_{16}O_2$	Nyasol	Zhimu
24	17.49	471.2027	471.5273	0.32	$C_{26}H_{30}O_8$	Obaculactone	Huangbo
25	17.60	741.4406	741.9373	0.50	$C_{39}H_{64}O_{13}$	Timosaponin A-III	Zhimu
26	18.38	455.2066	455.5279	0.32	$C_{26}H_{30}O_7$	Obacunone	Huangbo

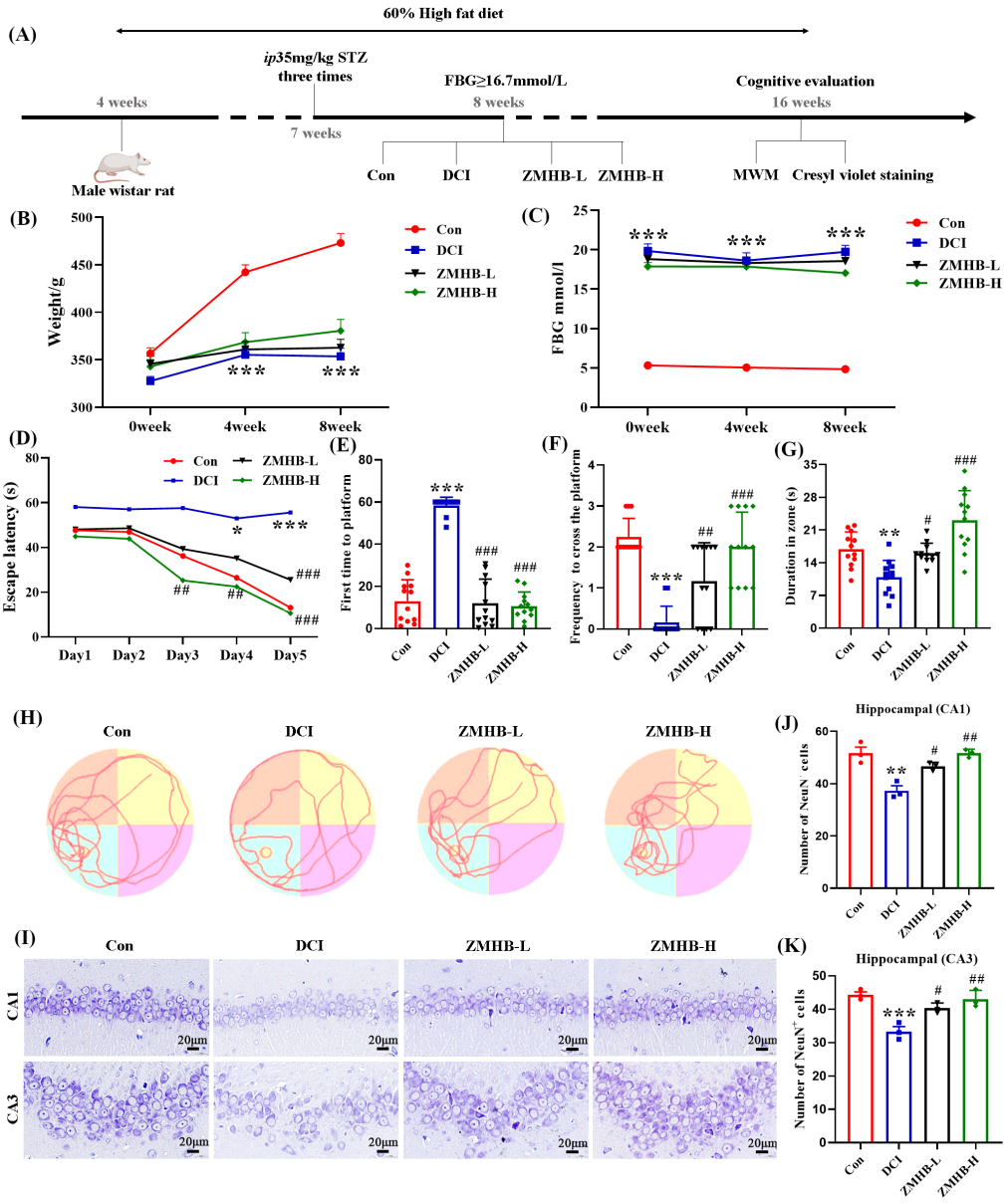

Figure 2. ZMHB improved the cognitive function of DCI rats. (**A**) Experimental workflow: Diabetic rats (induced by HFD + STZ, blood glucose concentration ≥ 16.7 mmol/L at 1 week post-modeling) were randomized into the DCI, ZMHB-L (2.16 g/kg), and ZMHB-H (4.32 g/kg) groups. (**B**) Body weights. (**C**) FBG. (**D–H**) Learning and memory functions were assessed by the MWM test after 8 weeks of treatment, including (**D**) 5-day escape latency during training and probe trial parameters after platform removal on Day 6: (**E**) first platform crossing latency, (**F**) frequency to cross the platform, (**G**) duration in target quadrant, and (**H**) representative swimming trajectories (n = 12). (**I**) Cresyl violet staining of the hippocampal CA1 and CA3 regions; scale bar = 20 μm (63×). (**J**) Neuronal count in CA1 (n = 3). (K) Neuronal count in CA3 (n = 3). The data are expressed as the means ± SDs. $^{*}P < 0.05$, $^{**}P < 0.01$, and $^{***}P < 0.001$ compared with the Con group; $^{\#}P < 0.05$, $^{\#\#}P < 0.01$, and $^{\#\#\#}P < 0.001$ compared with the DCI group.

(Figure 2E). Moreover, compared with Con rats, the DCI rats displayed fewer platform crossings and shorter dwell times in the target quadrant (Figures 2F and 2G). In contrast, ZMHB-treated rats exhibited significantly increased crossing frequencies and quadrant dwell times (Figures 2F and 2G). The results of the swimming trajectory analysis further supported these findings: Con rats persistently navigated toward the original platform position, whereas DCI rats swam irregularly. Strikingly, ZMHB-L- and ZMHB-H-treated animals showed improved directional movements and purposeful navigation (Figure 2H). Hippocampal CA1 and CA3 neuronal damage critically contributes to cognitive impairment. Cresyl violet staining revealed that the hippocampal neurons in the CA1 and CA3 regions of the DCI group were disorganized in terms of arrangement, reduced in number (Figures 2I-2K), irregular in morphology, and unevenly stained. However, the neurons in each treatment group were arranged neatly, their numbers significantly increased (Figures 2I-2K), their morphology was regular, and their staining was uniform. In summary, ZMHB alleviated cognitive dysfunction and hippocampal neuronal damage in a dose-dependent manner, with the efficacy of ZMHB-H

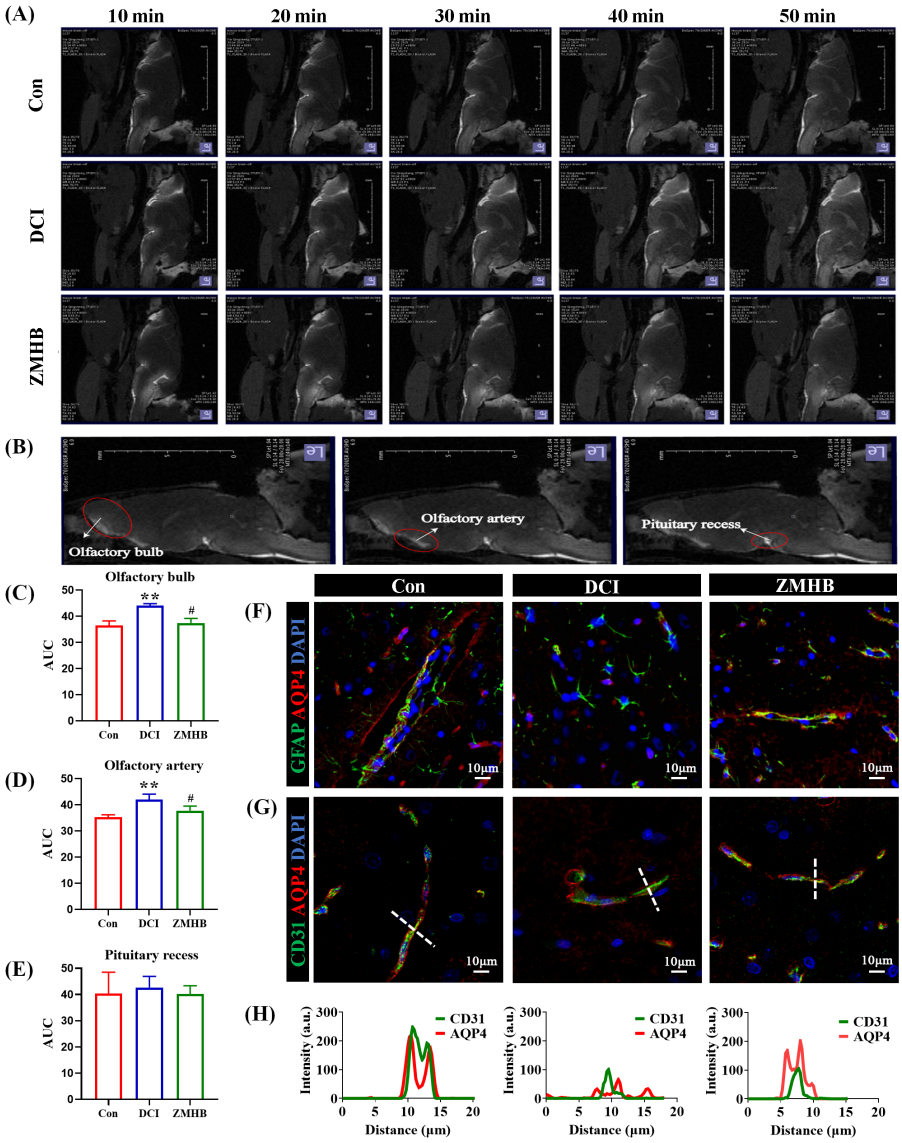

Figure 3. ZMHB enhanced GS clearance in DCI rats by maintaining AQP4 polarization. (**A**) Glymphatic system clearance function. (**B**) Gd-DTPA clearance rate. (**C-E**) Area under the curve (AUC) (n = 3). (**F**) Representative immunofluorescence images of the polarized distribution of AQP4 (red) in GFAP-positive astrocytes (green) within the cerebral cortex; scale bar = 10 μm (40×). (**G**) Representative immunofluorescence images of perivascular colocalization between AQP4 (red) and CD31 endothelial cells (green) in the cerebral cortex; scale bar = 10 μm (40×). (**H**) Quantitative expression of AQP4 under 20 μm vessel length. Data are expressed as the means ± SDs. $^{**}P < 0.01$ compared with the Con group; $^{\#}P < 0.05$ compared with the DCI group.

superior to that of ZMHB-L; thus, ZMHB-H was selected for subsequent investigations.

3.3. ZMHB enhanced GS clearance in DCI rats by maintaining AQP4 polarization

Modern medicine posits that impaired GS clearance constitutes the primary cause of learning and memory decline in diabetic rats (*6*), a mechanism congruent with the TCM pathogenesis theory of "toxin damaging brain collaterals". We detected GS clearance functioning through MRI, and the results revealed that in the Con group, the Gd-DTPA signal intensity peaked within 10-20 min post-injection and gradually decreased from 20 min onward. In contrast, the DCI group exhibited a peak Gd-DTPA signal intensity at 30 min post-injection, with no decreasing trend observed during the detection period, indicating a reduced cerebrospinal fluid–interstitial fluid (CSF–ISF) transport rate (Figure 3A). Additionally, the DCI group showed a significantly increased area under the curve (AUC) of the Gd-DTPA signal intensity in the olfactory bulb and olfactory artery regions, reflecting a decreased clearance rate and confirming GS dysfunction (Figures 3B-3E). Compared with the DCI group, the ZMHB group demonstrated a peak signal intensity at 20 min post-injection followed by a gradual decrease, a significantly increased CSF–ISF exchange rate (Figure 3A), markedly reduced AUC values in the olfactory

bulb and olfactory artery regions, and an increased Gd-DTPA clearance rate, suggesting that ZMHB improves GS clearance function (Figures 3B-3E). Considering that the distribution of AQP4 in perivascular astrocyte endfeet was the key histological basis of GS, we explored whether AQP4 participated in the regulation of DCI. Immunofluorescence analysis revealed that DCI rats exhibited a loss of polarized AQP4 distribution at perivascular astrocyte endfeet (GFAP), characterized by diffuse depolarized localization away from CD31-labeled vascular interfaces. ZMHB treatment restored astrocytic AQP4 polarization, as evidenced by AQP4 enrichment at perivascular endfeet (Figures 3F-3H). These findings indicate that ZMHB prevents and treats cognitive impairment by preserving AQP4 polarization to increase the clearance capacity of GS.

3.4. ZMHB restored AQP4 polarization in DCI rats through the exosomal pathway

Building on previous findings from our research group demonstrating that exosomes regulate AQP4 polarization to influence GS functionality (*24*), in this study, ZMHB was coadministered with the exosome release inhibitor GW4869 to elucidate the necessity of the exosomal pathway in the ZMHB-mediated restoration of AQP4 polarization. MWM tests demonstrated that ZMHB + GW4869 cotreatment abolished the ZMHB-induced improvements in learning and memory, as evidenced by prolonged escape latencies (Figure 4A), extended times to first reach the platform location (Figure 4B), reduced platform crossing frequencies (Figure 4C), shorter dwell times in the target quadrant (Figure 4D), and disorganized swimming trajectories (Figure 4E). Furthermore, GW4869 intervention eliminated the neuroprotective effects of ZMHB on hippocampal CA1/CA3 neurons, as shown by reduced neuronal density (Figures 4F-4H). Concurrently, ZMHB-induced restoration of AQP4 polarization at perivascular astrocyte endfeet was reversed, characterized by diffuse AQP4 distribution throughout astrocytes rather than localized perivascular clustering (Figures 4I-4K). These findings confirm that the exosomal pathway is essential for the ability of ZMHB to restore AQP4 polarization in DCI rats.

3.5. ZMHB ameliorated AQP4 depolarization in DCI rats by regulating serum-derived exosomal TIMP3-mediated MMP9/β-DG pathway

Circulating sExos are among the important sources of brain exosomes (*25*). To further investigate the mechanism of sExos in DCI, we isolated exosomes from the serum of experimental rats and characterized them using TEM, NTA, and western blotting. The sExos formed a double-layered membrane with a size distribution of 30–150 nm (Figures 5A and 5B), and tested positive for the exosome marker proteins, CD81 and TSG101 (Figure 5C). In summary, the circulating serum particles conformed to the characteristics of exosomes.

To elucidate the molecular mechanisms by which sExos regulate AQP4 polarization, we performed proteomics on the Con-sExos, DCI-sExos, and ZMHB-sExos groups. The results revealed 26 significantly upregulated proteins and 4 downregulated proteins in the ZMHB-sExos group, with TIMP3 expression markedly upregulated (Figure 5D-5F). The polarization of AQP4 is closely related to that of MMP9 (*13*), and TIMP3 is a natural inhibitor of MMP9 that can inhibit the activity of MMP9 and protect β-DG from degradation, thus supporting the polarization and function of AQP4. On the basis of the anchoring structure of AQP4 polarization and literature evidence, this study focused on the key protein TIMP3. Western blotting validation revealed that ZMHB significantly upregulated TIMP3 expression in the sExos group compared with that in the DCI-sExos group (Figures 5G and 5H), which is consistent with the proteomic findings. To explore how ZMHB restores AQP4 polarization in DCI rats, particularly its effects on the TIMP3-MMP9/β-DG pathway, we further analyzed the protein expressions in brain tissue. Western blotting results demonstrated that ZMHB intervention upregulated TIMP3 expression (Figures 5I and 5J) but downregulated the expressions of MMP9 and cleaved β-DG (Figures 5K-5N). Dual immunofluorescence staining of TIMP3/GFAP and β-DG/AQP4 revealed that ZMHB restored TIMP3 expression in astrocytes and enhanced β-DG-AQP4 colocalization (Figure 5O-5Q). These findings collectively suggest that ZMHB maintains astrocytic AQP4 polarization in DCI rats *via* the TIMP3-MMP9/β-DG pathway.

3.6. *In vitro* overexpression of TIMP3 improved the depolarization of AQP4 in astrocytes

To further validate the effects of serum exosomal TIMP3 on astrocytic AQP4 polarization, we induced a high-glucose injury model in astrocytes (Figure 6A) and treated both the Con and M groups with PKH26-labeled sExos (red fluorescence) for 24 h. Fluorescence imaging demonstrated effective exosome uptake by astrocytes, as indicated by the red intracellular signal (Figure 6C). The western blotting results demonstrated that the high-glucose environment both significantly suppressed TIMP3 expression in astrocytes and activated the abnormal MMP9-mediated β-DG cleavage pathway, leading to abnormally elevated ratios of the expressions of the AQP4 polarity markers M1/M23 (Figures 6D-6I). Notably, ZMHB-sExos and the TIMP3 small-molecule agonist MPT0B390 specifically upregulated TIMP3 protein levels, inhibited MMP9 activity, blocked β-DG cleavage, and ultimately restored the distribution of AQP4 polarization (Figures 6D-6I). Immunofluorescence

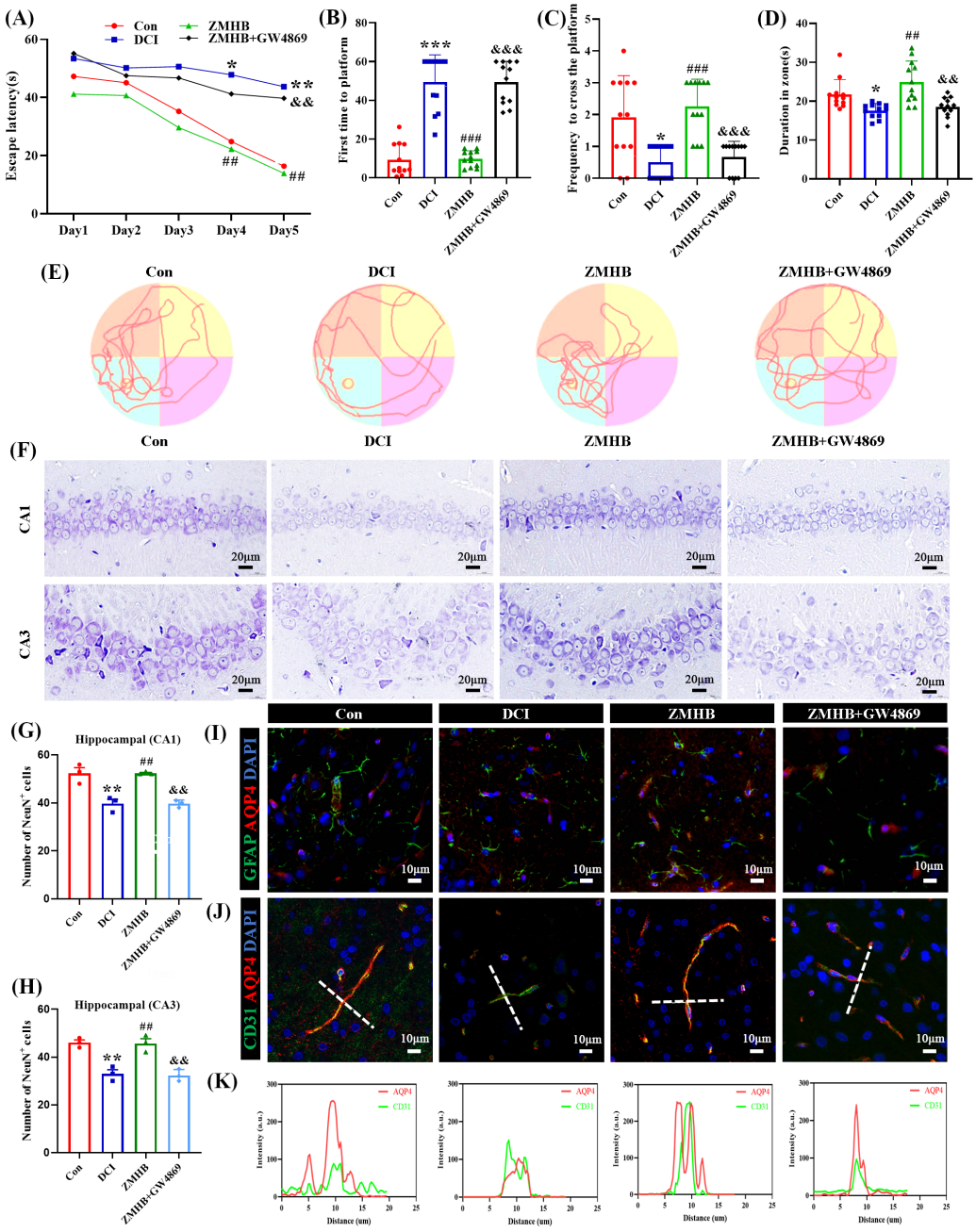

Figure 4. ZMHB restored AQP4 polarization in DCI rats through the exosomal pathway. Diabetic rats were randomized into DCI, ZMHB (4.32 g/kg), and ZMHB + GW4869 (4.32 g/kg + 1 mg/kg) groups. (**A-E**) Learning and memory functions were assessed by the MWM test after 8 weeks of treatment, including (**A**) 5-day escape latency during training and probe trial parameters after platform removal on Day 6: (**B**) first platform crossing latency, (**C**) frequency to cross the platform, (**D**) duration in target quadrant, and (**E**) representative swimming trajectories (n = 12). (**F**) Cresyl violet staining of the hippocampal CA1 and CA3 regions; scale bar = 20 μm (63×). (**G**) Neuronal count in CA1 (n = 3). (**H**) Neuronal count in CA3 (n = 3). (**I**) Representative immunofluorescence images of the polarized distribution of AQP4 (red) in GFAP-positive astrocytes (green) within the cerebral cortex; scale bar = 10 μm (40×). (**J**) Representative immunofluorescence images of perivascular colocalization between AQP4 (red) and CD31 endothelial cells (green) in the cerebral cortex; scale bar = 10 μm (40×). (**K**) Quantitative expression of AQP4 under 20 μm vessel length. Data are expressed as the means ± SDs. $^{*}P < 0.05$, $^{**}P < 0.01$, and $^{***}P < 0.001$ compared with the Con group; $^{\#\#}P < 0.01$ and $^{\#\#\#}P < 0.001$ compared with the DCI group; $^{\&\&}P < 0.01$ and $^{\&\&\&}P < 0.001$ compared with the ZMHB group.

staining further verified that ZMHB-sExos and MPT0B390 reversed the reduced expressions of AQP4, TIMP3, and β-DG that were caused by the high-glucose environment (Figures 6J and 6K). These findings establish the central role of the TIMP3-MMP9/β-DG pathway in the AQP4 polarization-mediated functional regulation of astrocytes.

4. Discussion

This study aimed to investigate the pathogenesis of DCI and the therapeutic effects of ZMHB from the perspective of the exosomal pathway. The results provide evidence that 1) ZMHB restored AQP4 polarization in DCI rats; 2) the exosomal pathway was essential for the ZMHB-

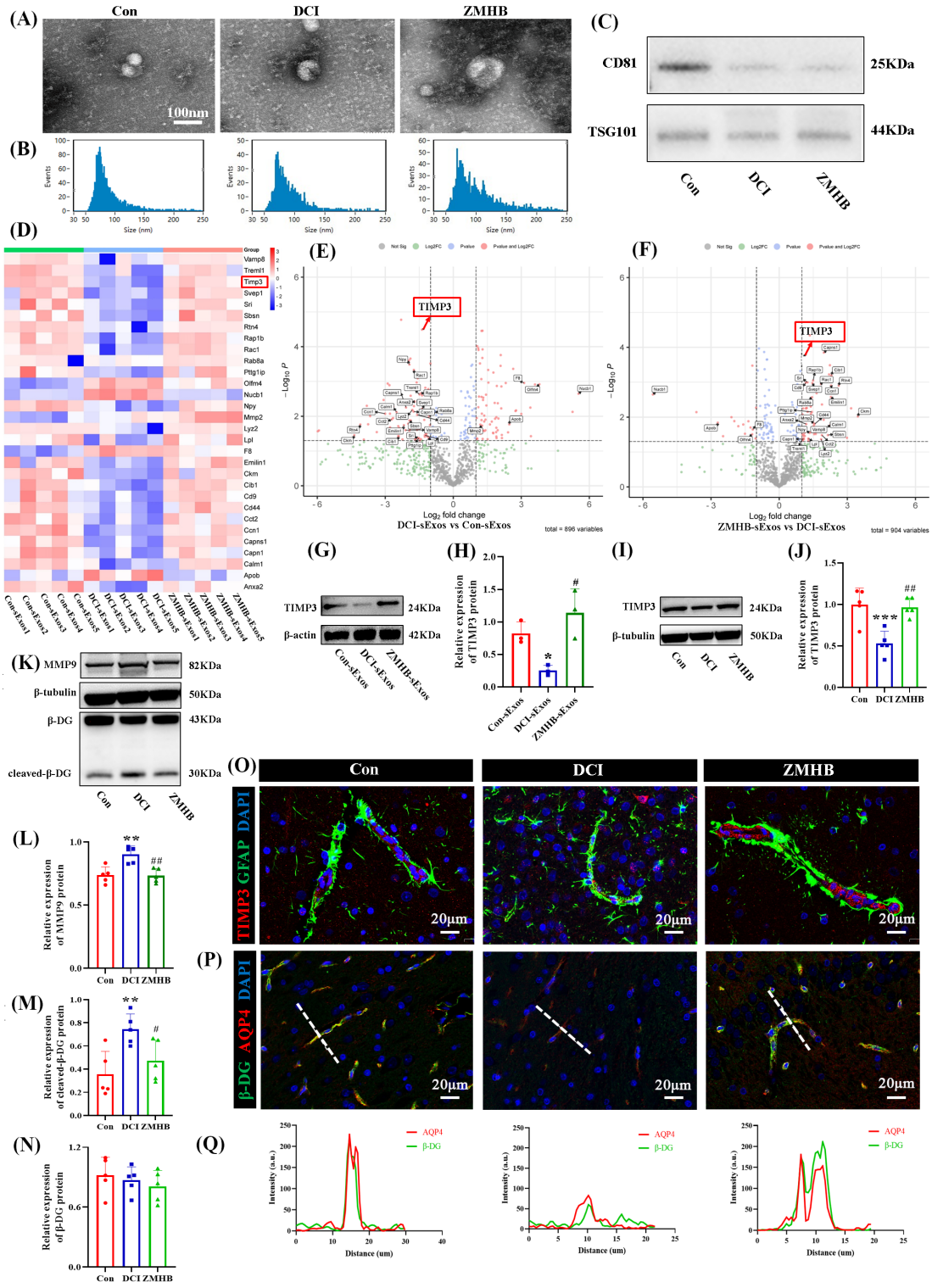

Figure 5. ZMHB ameliorated AQP4 depolarization in DCI rats by upregulating the serum-derived exosomal TIMP3-mediated MMP9/β-DG pathway. (**A**) Representative electron micrographs of sExos; scale bar = 100 nm. (**B**) Particle size distribution of sExos. (**C**) Expressions of the serum exosomal marker proteins CD81 and TSG101 ($n = 3$). (**D**) Hierarchical clustering heatmap of serum exosomal proteome profiles across the Con, DCI, and ZMHB groups, with red indicating higher expressions and blue indicating lower expressions ($n = 5$). (**E** and **F**) Volcano plot of differentially expressed exosomal proteins in DCI-sExos *vs.* Con-sExos (**E**) and in ZMHB-sExos *vs.* DCI-sExos (**F**), with the right quadrant indicating upregulated proteins (log2FC > 1, $P < 0.05$) and the left quadrant indicating downregulated proteins (log2FC < -1, $P < 0.05$) ($n = 5$). (**G** and **H**) The expressions of TIMP3 in sExos were detected by western blotting ($n = 3$). (**I** and **J**) TIMP3 expressions in whole-brain tissue were detected by western blotting ($n = 5$). (**K-N**) MMP9, cleaved-β-DG and β-DG expressions ($n = 5$) in whole-brain tissue were detected by western blotting. (**O**) TIMP3 (red) and GFAP (green) in cortical tissue sections from each group of rats were subjected to dual fluorescence staining; scale bar = 20 μm (40×). (**P**) The colocalization of AQP4 (red) and β-DG (green) in cortical tissue sections from rats in each group was determined using dual fluorescence staining; scale bar = 20 μm (40×). (**Q**) Linear intensity profiles of AQP4 and β-DG along 20 μm cortical regions (white dashed lines in P figure). Data are expressed as the means ± SDs. $^{*}P < 0.05$, $^{**}P < 0.01$, and $^{***}P < 0.001$ compared with the Con group; $^{\#}P < 0.05$ and $^{\#\#}P < 0.01$ compared with the DCI group.

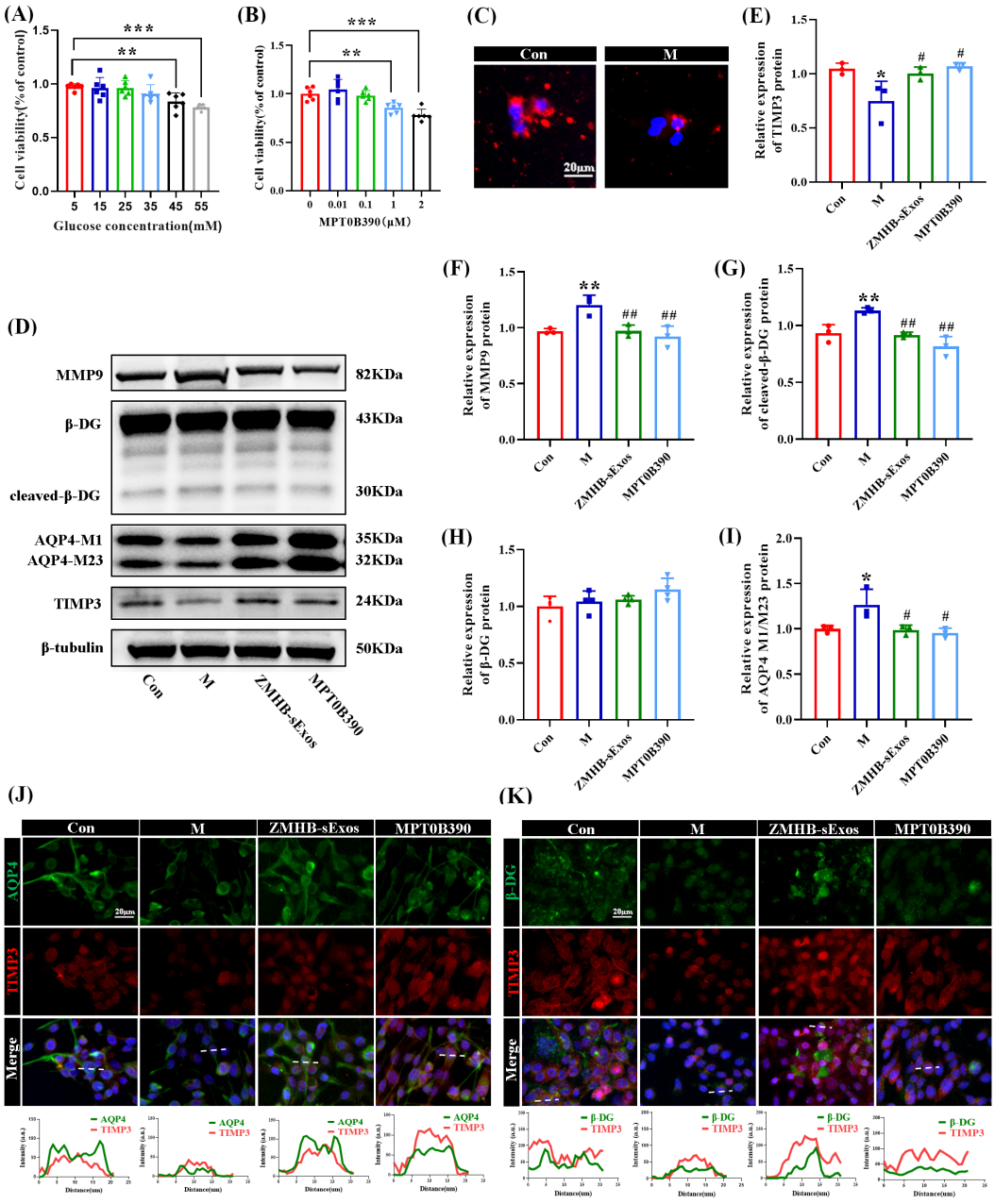

Figure 6. *In vitro* overexpression of TIMP3 improved the depolarization of AQP4 in astrocytes. (**A**) Murine astrocytes were subjected to glucose gradient screening (5–55 mM, 24 h) to induce hyperglycemic injury. The 45 mM dose (M: Model group) was determined to be optimal *via* a CCK-8 viability assay ($n = 6$). (**B**) Murine astrocytes were treated with a TIMP3 overexpression agent (0–2 μM) for 24 h under normal conditions. 0.1 μM was identified as the safe concentration with no cytotoxicity ($n = 6$). (**C**) Immunofluorescence analysis of the internalization of PKH26-labeled circulating serum-derived exosomes (red) by astrocytes. (**D-I**) TIMP3 (**E**), MMP9 (**F**), cleaved-β-DG (**G**), β-DG (**H**) and AQP4 M1/M23 (**I**) expression in astrocytes was detected by western blotting ($n = 3$). (**J-K**) Dual-labeling immunofluorescence analysis of protein colocalization in murine astrocytes. (**J**) AQP4 (green) and TIMP3 (red) colocalization after treatment with ZMHB-sExos or TIMP3 overexpression; scale bar = 20 μm (40×). (**K**) β-DG (green) and TIMP3 (red) colocalization after treatment with ZMHB-sExos or TIMP3 overexpression; scale bar = 20 μm (40×).

mediated restoration of AQP4 polarization in DCI rats; and 3) ZMHB upregulated peripheral exosomal TIMP3 expression and inhibited MMP9-mediated aberrant cleavage of β-DG, thereby restoring AQP4 polarization. These results not only confirm that dysregulated TIMP3-MMP9/β-DG/AQP4 signaling mediated by peripheral exosomes underlies DCI pathology but also demonstrate the potential of ZMHB as a therapeutic agent targeting this pathway. This study elucidates the modern scientific connotation of TCM pathogenesis "toxin damaging brain collaterals" from the perspective of AQP4 depolarization-mediated GS dysfunction, while identifying TIMP3 as a potential therapeutic target for reversing cognitive impairment in DCI patients.

Although ZMHB did not significantly affect body weight or FBG in DCI rats, it effectively alleviated neuronal damage and improved cognitive function. This therapeutic mechanism may involve the regulation of

hyperglycemia-induced pathological cascades by ZMHB, thereby improving cognitive function.

Related studies have shown that the clearance rate of interstitial fluid in the hippocampus and hypothalamus of diabetes patients is slow and that the function of the GS is abnormal, which may be an important reason for cognitive dysfunction (*8,26*). Most previous studies have focused on treating cognitive impairment by blocking the production of toxic substances such as amyloid-β (Aβ) (*27-29*), phosphorylated tau proteins (*30*), and advanced glycation end products (AGEs) (*31*) in brain tissue. In fact, these approaches have shown limited efficacy in halting cognitive decline. Recent evidence has indicated that diabetes may induce AQP4 depolarization in perivascular astrocytes (*32,33*), characterized by diffuse redistribution of AQP4 throughout the astrocytic soma (rather than polarized localization at perivascular endfeet) and an increased abundance of freely mobile tetrameric AQP4-M1 isoforms. This pathological redistribution disrupts cerebrospinal fluid flow dynamics, reduces the clearance efficiency of metabolic waste, and promotes the accumulation of toxic aggregates. Maintaining AQP4 polarization at astrocytic endfeet could restore GS inflow–outflow balance, increase cerebrospinal–interstitial fluid exchange, and provide a novel strategy for toxin clearance, offering new perspectives for preventing cognitive impairment. Guided by this premise, we investigated the association between AQP4 dysregulation-mediated GS dysfunction and DCI progression. Mechanistically, ZMHB ameliorates DCI by promoting AQP4 polarization to restore the GS clearance efficiency, which aligns with the TCM pathogenesis of "toxin damaging brain collaterals", potentially establishing the modern pathological basis for this TCM theory. Nevertheless, the regulatory mechanisms underlying AQP4 spatial redistribution in DCI require further exploration.

Previous studies have confirmed the pharmacological efficacy of ZMHB in restoring the distribution of AQP4 polarization in DCI rats, but its limited bioavailability in the brain (*34*), suggests that this effect may be mediated through peripheral regulatory mechanisms. Additionally, research has demonstrated that peripheral-derived exosomes can mediate GS clearance function by regulating the distribution of AQP4 polarization (*24*). For example, Wang *et al.* suggested that peripheral adipose tissue-derived exosomes could cause synaptic loss and cognitive impairment (*35*). On the basis of these findings, we investigated the role of the exosomal pathway in the ZMHB-mediated maintenance of AQP4 polarization by coadministering ZMHB with the exosome release inhibitor GW4869. The results showed that GW4869 partially decreased the efficacy of ZMHB in maintaining AQP4 polarization, consequently diminishing its ability to improve cognition and provide neuroprotection in DCI rats. These findings confirm that the delivery of peripheral-derived exosomes into the brain is critical for the ability of ZMHB to restore the distribution of AQP4 polarization.

Exosomes can achieve intercellular information transmission (*36-38*) by transferring various substances such as functional proteins, nucleic acids, and lipids (*39*). This study focused on exosomal functional proteins, and through proteomics screening, it was found that 26 proteins were significantly upregulated and 4 proteins were downregulated in the ZMHB-sExos group, with TIMP3 expression being significantly upregulated. Previous studies have shown that the distribution of polarized AQP4 partially depends on the complete dystroglycan complex (DGC)-like complex, which includes β-DG, α-synaptic nutrients, and dystrophin protein 71 (Dp71) (*40*). Si *et al.* reported that stable binding of β-DG to AQP4 could maintain polarization on the terminal feet of astrocytes (*13*). Mutations or defects in β-DG lead to impaired localization and function of AQP4, highlighting the importance of β-DG in anchoring AQP4 (*41*). The matrix metalloproteinase MMP9 degrades extracellular matrix (ECM) components. TIMP3 is a natural inhibitor of MMP9, which can inhibit the activity of MMP9, protect β-DG from degradation, and maintain the connection between cells and the ECM, thus supporting the polarization and function of AQP4. Multiple studies have shown that β-DG can be cleaved by MMP9 in various disease models (*15,16,42*). Under pathological conditions, downregulation of MMP9 blocker TIMP3 could activate MMP9. Combined with the anchoring structure of AQP4 polarization and existing evidence in the literature, our findings indicate that TIMP3 in circulating sExos is a key protein that regulates AQP4 polarization. ZMHB specifically upregulated TIMP3 levels in both sExos and brain tissues, which is consistent with the proteomics results. We therefore propose that brain-targeted delivery of serum-derived exosomal TIMP3 constitutes the central mechanism through which ZMHB maintains AQP4 polarization and alleviates DCI. Through *in vivo* experiments, we further investigated the regulatory effects of ZMHB on the TIMP3-MMP9/β-DG pathway. The results demonstrated that ZMHB promoted the entry of TIMP3 from circulating sExos into the brain, preventing β-DG from being cleaved by MMP9 and thereby maintaining the polarization of AQP4 in astrocytes. Overall, our data support the hypothesis that ZMHB restores AQP4 depolarization in DCI rats by modulating the exosomal TIMP3-mediated MMP9/β-DG pathway.

It should be noted that the primary aim of this study was to validate the existence of the "TIMP3-MMP9/β-DG-AQP4" signaling axis at a core level. While the high-glucose-treated astrocyte model used herein, as a classic *in vitro* system, provided key evidence supporting this central mechanism, we clearly recognize that this monoculture model cannot fully recapitulate the complexity of multicellular interactions within the

neurovascular unit (NVU)—such as those involving vascular endothelial cells, microglia, and neurons—in the *in vivo* DCI environment. For instance, the absence of brain microvascular endothelial cells, which play critical roles in blood-brain barrier (BBB) function, cytokine secretion, and responses to hyperglycemic stress, underscores the necessity for future studies to employ more complex models to explore the complete regulatory network of this pathway within the NVU. Therefore, utilizing co-culture models of astrocytes with brain microvascular endothelial cells or microglia, and even developing three-dimensional brain organoid models, will be important future directions for comprehensively elucidating this signaling axis. Notwithstanding these limitations, the evidence obtained from our simplified high-glucose astrocyte model still provides preliminary yet crucial support for the central role of serum exosomal TIMP3. To further confirm the effects of serum exosomal TIMP3 on astrocytic AQP4 polarization, MPT0B390 was applied to astrocytes, revealing that TIMP3 is a critical target for AQP4 polarization. Treatment of astrocytes with sExos specifically increased TIMP3 protein levels, inhibited MMP9 activity, blocked β-DG cleavage, and ultimately restored the distribution of AQP4 polarization. These findings establish the central role of the TIMP3-mediated MMP9/β-DG pathway in regulating astrocyte functions that are mediated by AQP4 polarization.

This study focuses on elucidating the integrated mechanism by which the TCM formula ZMHB alleviates DCI through the exosomal TIMP3-MMP9/β-DG-AQP4 axis. It is important to note that as a multi-component system, a comprehensive understanding of ZMHB's pharmacological material basis relies on in-depth analysis of its single active ingredients. Existing research suggests that common constituents of ZMHB (such as alkaloids, flavonoids, and saponins) possess the potential to regulate intercellular communication *via* exosomal pathways. For instance, berberine, a typical alkaloid, has been shown to modulate miR-182-5p expression in astrocyte-derived exosomes in neurological disease models, thereby suppressing neuroinflammation (*43*). In the context of diabetic nephropathy, it also inhibits the high glucose-induced transfer of TGFβ1 from mesangial cells to podocytes *via* exosomes, protecting podocyte function (*44*). Furthermore, Zhao *et al.* found that berberine-containing herbs can modulate changes in insulin target organs by downregulating miR-29-b, exerting anti-diabetic effects (*45*). Notably, the regulation of MMP activity *via* exosomes represents a common mechanism shared by multiple active components. For example, the primary flavonoid component of *Scutellaria baicalensis*, baicalein, has been demonstrated to effectively inhibit the expression of MMP-2 and MMP-9 in various pathological models, which provides mechanistic insight into how flavonoid components may stabilize the extracellular matrix and protect neurological function through the regulation of MMPs (*46,47*). Similarly, saponin components also exhibit the ability to influence pathological processes through exosomes. In studies on ginsenosides, Ginsenoside Rg1 (Rg1) can induce mesenchymal stem cells to secrete exosomes containing the NOTCH1 ring, promoting macrophage M2 polarization *via* NOTCH signaling activation and thereby ameliorating diabetic cardiomyopathy (*48*). Concurrently, Rg1 can inhibit exosomal miR-21 release, enhance TIMP3 expression, and regulate MMP activity, consequently protecting BBB integrity (*49*)—a mechanism that shows significant relevance and convergence with the TIMP3-MMP9/β-DG-AQP4 axis central to this study. In summary, future research should integrate techniques such as UPLC–Q–TOF–MS to systematically analyze the chemical composition of ZMHB and further screen for key active components using *in vitro* models to validate their upstream regulatory effects on exosomal TIMP3. This research path, progressing from the "holistic formula" to "single components", will deepen the understanding of the modernized mechanisms of TCM.

In summary, we demonstrated that exosomal protein transfer-mediated regulation of AQP4 depolarization-induced GS dysfunction constitutes the pathological mechanism of the TCM theory, "toxin damaging brain collaterals". ZMHB regulates the expression of TIMP3 in circulating sExos and its uptake in the brain, thereby restoring AQP4 polarization through the MMP9/β-DG pathway, improving GS function, and preventing DCI. These findings establish a modern scientific framework for the TCM pathogenesis of "toxin damaging brain collaterals" in DCI and provide a novel therapeutic strategy for its prevention and treatment.

Certainly, the current research also has several limitations. The primary issue is that the upstream molecular mechanisms through which ZMHB regulates TIMP3 remain unresolved. Second, an important unresolved aspect is that the existence of an exosomal cargo component (*e.g.*, miRNA)-AQP4 regulatory axis remains to be conclusively established. Furthermore, the cellular origins of the peripherally derived exosomes need to be systematically elucidated. Finally, it should be noted that, although this study confirmed at the cellular level that ZMHB-sExos can regulate AQP4 polarization *via* the TIMP3-MMP9/β-DG pathway, it did not directly verify through *in vivo* experiments whether peripheral injection of ZMHB-sExos alone is sufficient to fully recapitulate the overall therapeutic efficacy of ZMHB.

To address the aforementioned limitations, future research could proceed as follows: Regarding the upstream regulatory mechanisms, we speculate that ZMHB may increase TIMP3 synthesis by activating transcription factors (*e.g.*, SP1) or enhancing translation at the source cell level (*50*); or promote its selective sorting by modulating the ESCRT complex or sphingomyelinase activity during exosome biogenesis

(*51,52*). Subsequent mechanistic studies could be designed accordingly: for the first pathway, SP1 inhibitors or siRNA could be used in cellular models to observe whether ZMHB's upregulating effect is blocked; for the second pathway, changes in the expression or localization of key ESCRT proteins (*e.g.*, Alix, TSG101) following ZMHB treatment could be examined to verify their involvement. Meanwhile, to validate whether other regulatory components exist in exosomes, miRNA sequencing could be employed to unbiasedly screen for differentially expressed miRNAs in ZMHB-sExos, and dual-luciferase reporter assays, cellular functional experiments, and exosomal *in vivo* transfer techniques could be utilized to systematically verify whether they directly target AQP4 and affect its polarization. Elucidating the cellular origins of peripherally derived exosomes requires systematically investigating which cell types these TIMP3-enriched exosomes originate from. These exosomes likely derive from multiple metabolically active organs modulated by ZMHB: for example, adipocytes, which play a central role in energy metabolism and endocrine regulation and whose secreted exosomes have been confirmed to participate in adipose-brain communication (*53*); hepatocytes, as the primary sites of drug metabolism and protein synthesis, are a potential important source of exosomal TIMP3; mesenchymal stem cell-derived exosomes, reported to possess favorable biocompatibility and BBB crossing potential, are also candidate mediators in neurodegenerative disease research (*54*); additionally, blood cells and vascular endothelial cells are direct contributors to circulating exosomes. To this end, single-exosome multi-omics analysis, tissue-specific TIMP3 knockdown models, and CRISPR-based lineage tracing could be used to clarify their cellular origins. Most critically, it is essential to isolate sExos from the serum of ZMHB-treated donor animals, inject them alone into DCI model recipients, and comprehensively evaluate their effects on improving cognition and providing neuroprotection. These studies will establish a complete causal chain from peripheral regulation to central effects, comprehensively revealing the systemic mechanism of action of ZMHB.

5. Conclusion

In conclusion, this study confirmed that ZMHB could effectively alleviate cognitive dysfunction of in diabetic rats. Mechanistically, this study revealed that abnormal downregulation of TIMP3 triggers β-DG lysis, which is the molecular mechanism of AQP4 depolarization in DCI. Serum exosomal TIMP3 from the ZMHB group entered the brain, inhibiting the activity of MMP9 in astrocytes and preventing β-DG from being cleaved, thereby restoring the polarization of AQP4 and exerting neuroprotective effects on DCI. The results of this study indicate that ZMHB is effective and safe and may be a promising drug for treating DCI.

Acknowledgements

Zhimu and Huangbo were identified by professor Lin Ma (Tianjin University of Traditional Chinese Medicine).

Funding: This work was supported by the Foundation of National Natural Science Foundation of China (82174112), the Science and Technology Project of Haihe Laboratory of Modern Chinese Medicine (22HHZYSS00015), the State Key Laboratory of Component-based Chinese Medicine (CBQM2022102) and the Eyas Research Project of Tianjin University of Traditional Chinese Medicine (XJS2022207).

Ethics approval: This experiment passed the ethical review of animal experiments at Tianjin University of Traditional Chinese Medicine (TCM-LAEC2021152). All experiments were performed in accordance with relevant guidelines and regulations.

Conflict of Interest: The authors have no conflicts of interest to disclose.

References

1. Dove A, Shang Y, Xu W, Grande G, Laukka EJ, Fratiglioni L, Marseglia A. The impact of diabetes on cognitive impairment and its progression to dementia. Alzheimers Dement. 2021; 17:1769-1778.
2. Rizzo MR, Di Meo I, Polito R, Auriemma MC, Gambardella A, di Mauro G, Capuano A, Paolisso G. Cognitive impairment and type 2 diabetes mellitus: Focus of SGLT2 inhibitors treatment. Pharmacol Res. 2022; 176:106062.
3. Zanotto C, Simão F, Gasparin MS, Biasibetti R, Tortorelli LS, Nardin P, Gonçalves CA. Exendin-4 Reverses Biochemical and Functional Alterations in the Blood-Brain and Blood-CSF Barriers in Diabetic Rats. Mol Neurobiol. 2017; 54:2154-2166.
4. Baumgart M, Snyder HM, Carrillo MC, Fazio S, Kim H, Johns H. Summary of the evidence on modifiable risk factors for cognitive decline and dementia: A population-based perspective. Alzheimers Dement. 2015; 11:718-726.
5. Tuligenga RH, Dugravot A, Tabák AG, Elbaz A, Brunner EJ, Kivimäki M, Singh-Manoux A. Midlife type 2 diabetes and poor glycaemic control as risk factors for cognitive decline in early old age: a post-hoc analysis of the Whitehall II cohort study. Lancet Diabetes Endocrinol. 2014; 2:228-235.
6. Benveniste H, Liu X, Koundal S, Sanggaard S, Lee H, Wardlaw J. The Glymphatic System and Waste Clearance with Brain Aging: A Review. Gerontology. 2019; 65:106-119.
7. Kim YK, Nam KI, Song J. The Glymphatic System in Diabetes-Induced Dementia. Front Neurol. 2018; 9:867.
8. Zhang L, Chopp M, Jiang Q, Zhang Z. Role of the glymphatic system in ageing and diabetes mellitus impaired cognitive function. Stroke Vasc Neurol. 2019; 4:90-92.
9. Silva I, Silva J, Ferreira R, Trigo D. Glymphatic system,

AQP4, and their implications in Alzheimer's disease. Neurol Res Pract. 2021; 3:5.
10. Ward R, Li W, Abdul Y, Jackson L, Dong G, Jamil S, Filosa J, Fagan SC, Ergul A. NLRP3 inflammasome inhibition with MCC950 improves diabetes-mediated cognitive impairment and vasoneuronal remodeling after ischemia. Pharmacol Res. 2019; 142:237-250.
11. Ran Q, Tian H, Lin J, Wang H, Wang B, Chen Z, Song D, Gong C. Mesenchymal Stem Cell-Derived Exosomes: A Novel Approach to Diabetes-Associated Cognitive Impairment. J Inflamm Res. 2023; 16:4213-4228.
12. Jia L, Zhu M, Kong C, *et al*. Blood neuro-exosomal synaptic proteins predict Alzheimer's disease at the asymptomatic stage. Alzheimers Dement. 2021; 17:49-60.
13. Si X, Dai S, Fang Y, Tang J, Wang Z, Li Y, Song Z, Chen Y, Liu Y, Zhao G, Zhang B, Pu J. Matrix metalloproteinase-9 inhibition prevents aquaporin-4 depolarization-mediated glymphatic dysfunction in Parkinson's disease. J Adv Res. 2024; 56:125-136.
14. Jäkel L, Kuiperij HB, Gerding LP, Custers EEM, van den Berg E, Jolink WMT, Schreuder F, Küsters B, Klijn CJM, Verbeek MM. Disturbed balance in the expression of MMP9 and TIMP3 in cerebral amyloid angiopathy-related intracerebral haemorrhage. Acta Neuropathol Commun. 2020; 8:99.
15. Zhu B, Cao A, Chen C, Zhou W, Luo W, Gui Y, Wang Q, Xu Z, Wang J. MMP-9 inhibition alleviates postoperative cognitive dysfunction by improving glymphatic function *via* regulating AQP4 polarity. Int Immunopharmacol. 2024; 126:111215.
16. Yuan Y, Peng W, Lei J, Zhao Y, Zhao B, Li Y, Wang J, Qu Q. AQP4 Endocytosis-Lysosome Degradation Mediated by MMP-9/β-DG Involved in Diabetes Cognitive Impairment. Mol Neurobiol. 2024; 61:8438-8453.
17. Sun H, Li TJ, Sun LN, Qiu Y, Huang BB, Yi B, Chen WS. Inhibitory effect of traditional Chinese medicine Zi-Shen Pill on benign prostatic hyperplasia in rats. J Ethnopharmacol. 2008; 115:203-208.
18. Li XN, Zhang A, Sun H, Song Y, Zou D, Wang X. Rapid discovery of absorbed constituents and metabolites in rat plasma after the oral administration of Zi Shen Wan using high-throughput UHPLC-MS with a multivariate analysis approach. J Sep Sci. 2016; 39:4700-4711.
19. Xue A, Zhao D, Zhao C, Li X, Yang M, Zhao H, Zhao C, Lei X, Wu J, Zhang N. Study on the neuroprotective effect of Zhimu-Huangbo extract on mitochondrial dysfunction in HT22 cells induced by D-galactose by promoting mitochondrial autophagy. J Ethnopharmacol. 2024; 318:117012.
20. Shi J, Yin Q, Zhang L, Wu Y, Yi P, Guo M, Li H, Yuan L, Wang Z, Zhuang P, Zhang Y. Zi Shen Wan Fang Attenuates Neuroinflammation and Cognitive Function *Via* Remodeling the Gut Microbiota in Diabetes-Induced Cognitive Impairment Mice. Front Pharmacol. 2022; 13:898360.
21. Yin Q, Zhang L, Han X, Zhang H, Wang F, Qin X, Zhuang P, Zhang Y. Zi Shen Wan Fang regulates kynurenine metabolism to alleviate diabetes-associated cognitive impairment *via* activating the skeletal muscle PGC1α-PPARα signaling. Phytomedicine. 2022; 99:154000.
22. Valente T, Gella A, Solé M, Durany N, Unzeta M. Immunohistochemical study of semicarbazide-sensitive amine oxidase/vascular adhesion protein-1 in the hippocampal vasculature: pathological synergy of Alzheimer's disease and diabetes mellitus. J Neurosci Res. 2012; 90:1989-1996.
23. Sasaki-Hamada S, Sacai H, Oka JI. Diabetes onset influences hippocampal synaptic plasticity in streptozotocin-treated rats. Neuroscience. 2012; 227:293-304.
24. Zhang L, Li D, Yi P, Shi J, Guo M, Yin Q, Liu D, Zhuang P, Zhang Y. Peripheral origin exosomal microRNAs aggravate glymphatic system dysfunction in diabetic cognitive impairment. Acta Pharm Sin B. 2023; 13:2817-2825.
25. Saint-Pol J, Gosselet F, Duban-Deweer S, Pottiez G, Karamanos Y. Targeting and Crossing the Blood-Brain Barrier with Extracellular Vesicles. Cells. 2020; 9:851.
26. Jiang Q, Zhang L, Ding G, Davoodi-Bojd E, Li Q, Li L, Sadry N, Nedergaard M, Chopp M, Zhang Z. Impairment of the glymphatic system after diabetes. J Cereb Blood Flow Metab. 2017; 37:1326-1337.
27. Chen Z, Zhong C. Decoding Alzheimer's disease from perturbed cerebral glucose metabolism: implications for diagnostic and therapeutic strategies. Prog Neurobiol. 2013; 108:21-43.
28. Li H, Luo Y, Xu Y, Yang L, Hu C, Chen Q, Yang Y, Ma J, Zhang J, Xia H, Li Y, Yang J. Meloxicam Improves Cognitive Impairment of Diabetic Rats through COX2-PGE2-EPs-cAMP/pPKA Pathway. Mol pharmaceutics. 2018; 15:4121-4131.
29. Zhang T, Pan BS, Zhao B, Zhang LM, Huang YL, Sun FY. Exacerbation of poststroke dementia by type 2 diabetes is associated with synergistic increases of beta-secretase activation and beta-amyloid generation in rat brains. Neuroscience. 2009; 161:1045-1056.
30. Jayaraj RL, Azimullah S, Beiram R. Diabetes as a risk factor for Alzheimer's disease in the Middle East and its shared pathological mediators. Saudi J Biol Sci. 2020; 27:736-750.
31. Tang Y, Yu C, Wu J, Chen H, Zeng Y, Wang X, Yang L, Mei Q, Cao S, Qin D. Lychee seed extract protects against neuronal injury and improves cognitive function in rats with type II diabetes mellitus with cognitive impairment. Int J Mol Med. 2018; 41:251-263.
32. Chiu CD, Chen CC, Shen CC, Chin LT, Ma HI, Chuang HY, Cho DY, Chu CH, Chang C. Hyperglycemia exacerbates intracerebral hemorrhage *via* the downregulation of aquaporin-4: temporal assessment with magnetic resonance imaging. Stroke. 2013; 44:1682-1689.
33. Zhang L, Chopp M, Zhang Y, Xiong Y, Li C, Sadry N, Rhaleb I, Lu M, Zhang ZG. Diabetes Mellitus Impairs Cognitive Function in Middle-Aged Rats and Neurological Recovery in Middle-Aged Rats After Stroke. Stroke. 2016; 47:2112-2118.
34. Zheng Y, Zhang Y, Geng S, Xu M, Yin Q, Song L, Zhuang P, Zhang Y. Identification of the constituents and metabolites in rats after oral administration of Zi Shen Formula by UPLC-Q-TOF/MS combined pattern recognition analysis. Biomed Chromatogr. 2018; 32. doi: 10.1002/bmc.4060.
35. Wang J, Li L, Zhang Z, Zhang X, Zhu Y, Zhang C, Bi Y. Extracellular vesicles mediate the communication of adipose tissue with brain and promote cognitive impairment associated with insulin resistance. Cell Metab. 2022; 34:1264-1279.e1268.
36. Liu W, Bai X, Zhang A, Huang J, Xu S, Zhang J. Role of Exosomes in Central Nervous System Diseases. Front Mol Neurosci. 2019; 12:240.
37. Datta Chaudhuri A, Dasgheyb RM, DeVine LR, Bi H, Cole RN, Haughey NJ. Stimulus-dependent modifications

in astrocyte-derived extracellular vesicle cargo regulate neuronal excitability. Glia. 2020; 68:128-144.
38. Jean-Toussaint R, Tian Y, Chaudhuri AD, Haughey NJ, Sacan A, Ajit SK. Proteome characterization of small extracellular vesicles from spared nerve injury model of neuropathic pain. J Proteomics. 2020; 211:103540.
39. Lu Y, Zhang J, Han B, Yu Y, Zhao W, Wu T, Mao Y, Zhang F. Extracellular vesicles DJ-1 derived from hypoxia-conditioned hMSCs alleviate cardiac hypertrophy by suppressing mitochondria dysfunction and preventing ATRAP degradation. Pharmacol Res. 2023; 187:106607.
40. Waite A, Brown SC, Blake DJ. The dystrophin-glycoprotein complex in brain development and disease. Trends Neurosci. 2012; 35:487-496.
41. Gondo A, Shinotsuka T, Morita A, Abe Y, Yasui M, Nuriya M. Sustained down-regulation of β-dystroglycan and associated dysfunctions of astrocytic endfeet in epileptic cerebral cortex. J Biol Chem. 2014; 289:30279-30288.
42. Wang Z, Li Y, Wang Z, Liao Y, Ye Q, Tang S, Wei T, Xiao P, Huang J, Lu W. Edaravone Maintains AQP4 Polarity *Via* OS/MMP9/β-DG Pathway in an Experimental Intracerebral Hemorrhage Mouse Model. Mol Neurobiol. 2024; 61:7639-7658.
43. Ding W, Gu Q, Liu M, Zou J, Sun J, Zhu J. Astrocytes-derived exosomes pre-treated by berberine inhibit neuroinflammation after stroke *via* miR-182-5p/Rac1 pathway. Int Immunopharmacol. 2023; 118:110047.
44. Wang YY, Tang LQ, Wei W. Berberine attenuates podocytes injury caused by exosomes derived from high glucose-induced mesangial cells through TGFβ1-PI3K/AKT pathway. Eur J Pharmacol. 2018; 824:185-192.
45. Zhao HL, Sui Y, Qiao CF, *et al*. Sustained antidiabetic effects of a berberine-containing Chinese herbal medicine through regulation of hepatic gene expression. Diabetes. 2012; 61:933-943.
46. Chandrashekar N, Selvamani A, Subramanian R, Pandi A, Thiruvengadam D. Baicalein inhibits pulmonary carcinogenesis-associated inflammation and interferes with COX-2, MMP-2 and MMP-9 expressions *in-vivo*. Toxicol Appl Pharmacol. 2012; 261:10-21.
47. He HJ, Lv ZY, Li ZY, Zhang LY, Liao Q, Zheng HQ, Su WY, Rao SQ, Yu XB, Wu ZD. Efficacy of combined treatment with albendazole and baicalein against eosinophilic meningitis induced by Angiostrongylus cantonensis in mice. J Helminthol. 2011; 85:92-99.
48. Zhen J, Bai J, Liu J, Men H, Yu H. Ginsenoside RG1-induced mesenchymal stem cells alleviate diabetic cardiomyopathy through secreting exosomal circNOTCH1 to promote macrophage M2 polarization. Phytother Res. 2024; 38:1745-1760.
49. Zhai K, Duan H, Wang W, Zhao S, Khan GJ, Wang M, Zhang Y, Thakur K, Fang X, Wu C, Xiao J, Wei Z. Ginsenoside Rg1 ameliorates blood-brain barrier disruption and traumatic brain injury *via* attenuating macrophages derived exosomes miR-21 release. Acta Pharm Sin B. 2021; 11:3493-3507.
50. Bernot D, Barruet E, Poggi M, Bonardo B, Alessi MC, Peiretti F. Down-regulation of tissue inhibitor of metalloproteinase-3 (TIMP-3) expression is necessary for adipocyte differentiation. J Biol Chem. 2010; 285:6508-6514.
51. Vietri M, Radulovic M, Stenmark H. The many functions of ESCRTs. Nat Rev Mol Cell Biol. 2020; 21:25-42.
52. Hessvik NP, Llorente A. Current knowledge on exosome biogenesis and release. Cell Mol Life Sci. 2018; 75:193-208.
53. Wang J, Li L, Zhang Z, Zhang X, Zhu Y, Zhang C, Bi Y. Extracellular vesicles mediate the communication of adipose tissue with brain and promote cognitive impairment associated with insulin resistance. Cell Metab. 2022; 34:1264-1279.e8.
54. Kandeel M, Morsy MA, Alkhodair KM, Alhojaily S. Mesenchymal Stem Cell-Derived Extracellular Vesicles: An Emerging Diagnostic and Therapeutic Biomolecules for Neurodegenerative Disabilities. Biomolecules. 2023; 13:1250.

Received September 23, 2025; Revised November 25, 2025; Accepted December 6, 2025.

[§]These authors contributed equally to this work.

**Address correspondence to:*
Qingsheng Yin, Yanjun Zhang and Pengwei Zhuang, Tianjin University of Traditional Chinese Medicine, Jinghai District, Tianjin, 301617, China.
E-mail: carrysable@163.com (QSY), zyjsunye@163.com (YJZ) and zhuangpengwei@163.com (PWZ)

Released online in J-STAGE as advance publication December 17, 2025.